Effect of iron in silicon feedstock on *p*- and *n*-type multicrystalline silicon solar cells

G. Coletti, ^{1,a)} R. Kvande, ² V. D. Mihailetchi, ¹ L. J. Geerligs, ¹ L. Arnberg, ² and E. J. Øvrelid³

The effect of iron contamination in multicrystalline silicon ingots for solar cells has been investigated. Intentionally contaminated p- and n-type multicrystalline silicon ingots were grown by adding 53 ppm by weight of iron in the silicon feedstock. They are compared to reference ingots produced from nonintentionally contaminated silicon feedstock. p-type and n-type solar cell processes were applied to wafers sliced from these ingots. The as-grown minority carrier lifetime in the iron doped ingots is about 1–2 and 6–20 μ s for p and n types, respectively. After phosphorus diffusion and hydrogenation this lifetime is improved up to 50 times in the p-type ingot, and about five times in the n-type ingot. After boron/phosphorus codiffusion and hydrogenation the improvement is about ten times for the p-type ingot and about four times for the n-type ingot. The as-grown interstitial iron concentration in the p-type iron doped ingot is on the order of 10^{13} cm⁻³, representing about 10% of the total iron concentration in the ingot, and is reduced to below 10¹¹ cm⁻³ after phosphorus diffusion and subsequent hydrogenation. The concentration of interstitial iron after boron/phosphorus codiffusion and hydrogenation is about 10¹² cm⁻³, pointing out the reduced gettering effectiveness of boron/phosphorus codiffusion. The effect of the iron contamination on solar cells level is a decrease in the diffusion length in the top half of the ingots with a trend in agreement with Scheil's model for segregation. This is, however, not the only impact of the iron. An increased crystal defect concentration in the top and bottom of the Fe doped ingots, compared to the reference ingots, is observed, which contributes considerably to the degradation of the solar cell performance. © 2008 American Institute of Physics. [DOI: 10.1063/1.3021355]

I. INTRODUCTION

At the moment, the photovoltaic (PV) industry is facing a shortage in silicon feedstock. This has led to a steady introduction of less pure silicon. Also, it is expected that solar grade silicon made through the direct- or metallurgical purification route will become available on the market soon. Therefore, the PV industry should address the question how cell parameters are affected by, and cell processes can be best adapted to, less pure material which are the main topics of our present investigation.

The research performed in the 1980s by Westinghouse Corp¹ is still used as reference for the effect of impurities on solar cell performance. However, because of the modifications of cell processes since then and the increased use of multicrystalline cast ingots instead of single-crystalline ingots, there is a need for updated and more detailed studies.

Also, the earlier work of Westinghouse focused on solar cell efficiency. The minority carrier diffusion length on solar cell level was not directly measured but it was approximated by modeling of results. The diffusion length as a function of impurity concentration is the most reliable input parameter to model and predict impact in different cell architectures (e.g., different thickness, different surface passivation, etc.).

In this work we study the impact of Fe intentionally

a)Electronic mail: coletti@ecn.nl. FAX: +31 (0) 224 56 43 82.

introduced in the silicon feedstock on *p*-type and *n*-type multicrystalline silicon (mc-Si) ingots grown by directional solidification. We investigate its impacts at different stage of the solar cell manufacturing stage with emphasis on the properties of the solar cells in comparison to reference uncontaminated material. The diffusion length is determined directly from spatial resolved as well as average internal quantum efficiencies (IQEs) of the solar cells.

We choose to investigate Fe because it is a dominant metal impurity in silicon wafers. ^{2,3} Typical concentration of total Fe [Fe] in commercial multicrystalline silicon ingots from neutron activation analysis ^{4,5} (NAA) measurements has been reported ^{2,3} to be about in the range of $10^{13}-10^{15}$ cm⁻³. It is a relatively fast diffusing impurity ($D=2.6 \times 10^{-6}$ cm²/s at 1000 °C) (Ref. 6); thus it can be gettered.

It is important to note that the Fe we introduced in the silicon charge is, of course, subject to a similar thermal history and process as would be any Fe present as impurity in the feedstock. The thermal history of the material determines, among other aspects, the fraction of impurities which are electrically active in Si, the properties of precipitates, etc., and thus the final impact of impurities on the solar cell performance. Our experimental approach differs from previous works (e.g., Refs. 7 and 8) where Fe was introduced by ion implantation or intentional surface contamination on wafer level, followed by a thermal anneal of the wafer.

We discuss in this article the impact on solar cell perfor-

¹ECN Solar Energy, Westerduinweg 3, NL-1755 LE Petten, The Netherlands

²Norwegian University of Science and Technology, Alfred Getz vei 2, N-7491 Trondheim, Norway ³SINTEF Materials and Chemistry, Alfred Getz vei 2, N-7465 Trondheim, Norway

⁽Received 4 June 2008; accepted 7 October 2008; published online 21 November 2008)

TABLE I. Ingot descriptions. The dopant and the impurity that have been introduced in the silicon charge.

Label	Crucible	Coating	Dopant (ppm by weight)	Impurity (ppm by weight)
<i>p</i> -type reference	HP silica	Purified Si ₃ N ₄	B, 0.116	
p-type Fe	HP silica	Purified Si ₃ N ₄	B, 0.116	Fe, 53
n-type reference	HP silica	Purified Si ₃ N ₄	P, 0.318	• • •
<i>n</i> -type Fe	HP silica	Purified Si ₃ N ₄	P, 0.318	Fe, 53

mance while a separate article has described the distribution of Fe in the ingots. We believe our studies are representative and useful for assessment of the impact of unwanted Fe impurities in feedstock and crystallization materials.

In addition to showing the impact of Fe in multicrystalline cast ingots, this article also shows that the impact of impurities does not only cause a reduction in diffusion length due to interstitial Fe point defects but also seems to affect the crystallization process, contributing to a further reduction in the performance of the solar cells.

II. EXPERIMENTAL METHODS

Four pilot scale ingots have been grown for this study using a Crystalox DS 250 furnace designed to solidify multicrystalline ingots by Bridgman-type directional solidification method. This furnace allows growth of 12 kg ingots by the directional solidification method, having a diameter of 250 mm and a height of 110 mm. In order to study the impact of the intentionally introduced contaminant, other sources of contamination (e.g., feedstock, crucible, and coating) have been kept as low as possible. Thus, virgin polysilicon, high purity (HP) crucibles, ¹⁰ and purified Si₃N₄ (Ref. 11) have been used. The dopant and impurity were introduced in the feedstock charge according to Table I.

The amount of Fe introduced in the melt (53 ppm by weight) has been chosen targeting [Fe]= 3×10^{13} cm⁻³ at about three quarters of the ingot height, assuming an effective distribution coefficient equaling the equilibrium coefficient (6×10^{-6}). A full description of the crystallization process and comprehensive characterization of the material can be found in Ref. 9. A direct contact between ingot and crucible was observed in some regions of the *p*-type reference ingot. This resulted in interstitial oxygen (O_i) levels of about 4×10^{17} cm⁻³ in the middle of the ingot, decreasing toward the top. The O_i concentrations in the *p*-type and *n*-type Fe doped ingots are 1.5×10^{17} and 3×10^{17} cm⁻³, respectively, with uniform distribution. The $[O_i]$ in the *n*-type reference ingot is about 3×10^{17} cm⁻³.

The *n*-type reference ingot was grown (at an earlier point of time) under different furnace conditions. This resulted in a substitutional carbon concentration of about 7×10^{17} cm⁻³ in the top of the ingot. This has to be taken into account when interpreting the results from this ingot. The other ingots have a substitutional carbon concentration below 5×10^{17} cm⁻³.

From each ingot center a block of 125×125 mm² was cut, which was sliced into wafers with a thickness of

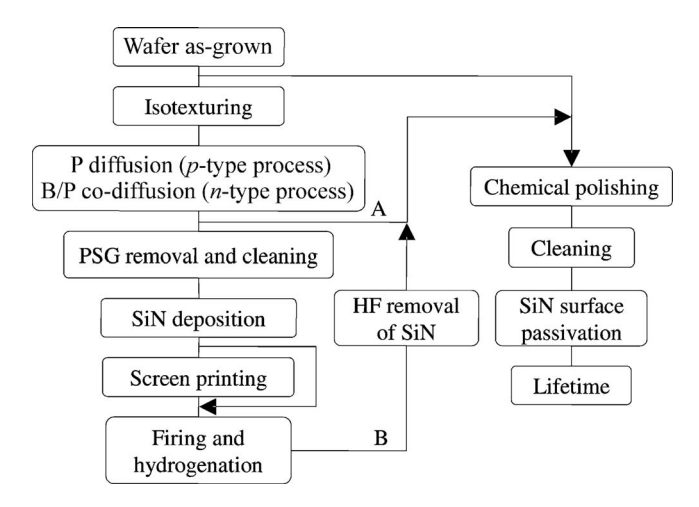


FIG. 1. Solar cell process steps. Wafers are taken out after gettering (a) and hydrogenation (b) to study the impact of each of these steps in comparison to as-grown wafers. The wafers after hydrogenation receive no screen printing. PSG denotes phosphosilicate glass.

240 μ m. A set of ten wafers for each ingot, representative of the complete ingot heights, were processed into solar cells with a baseline p-type and n-type solar cell process. The p-type solar cell process is the state of the art industrial P diffusion Al back surface field (BSF) SiN_x :H firing through. The n-type cell process consists of a boron front emitter and phosphorous BSF in a codiffusion step (B/P codiffusion), both passivated by SiN_x :H and firing through metallization with open rear side grid. The n-type cell process consists of a boron front emitter and phosphorous BSF in a codiffusion step (B/P codiffusion), both passivated by SiN_x :H and firing through metallization with open rear side grid.

Neighboring wafers were used to characterize the minority carrier lifetime after phosphorus (P) diffusion and hydrogenation ¹⁴ according to the scheme in Fig. 1. The samples to characterize the P diffusion were removed from the solar cell process after the emitter formation. The emitter was removed by a chemical polishing step (HF/HNO₃), followed by deposition of a SiN surface passivating layer ¹⁵ on both sides.

The samples to characterize the phosphorous diffusion and hydrogenation were removed from the normal process sequence after SiN_x : H antireflection coating (ARC) deposition. They were annealed under the same conditions as for the metallization firing through of the regular cells but without metal applied and with SiN_x : H deposited additionally on the rear side. Subsequently the SiN_x : H ARC was removed with HF. The emitter was etched by a chemical polishing step followed by deposition of SiN surface passivating layers on both sides. An equivalent procedure was performed to prepare lifetime test samples after B/P codiffusion and hydrogenation according to the n-type cell process. A set of vertically adjacent ("neighbor") wafers were polished and passivated with SiN under the same conditions as the other two sets to provide the lifetime on as-grown samples.

The surface passivating SiN layers, deposited at low temperature, do not change bulk properties ¹⁶ (hydrogen passivation) after deposition and assure a surface recombination velocity less than 50 cm/s, verified by reference float zone samples. Thus for high bulk lifetime, the effective minority carrier lifetime, which we report in this article, is an underestimation of the bulk lifetime. We use the notation "p-type

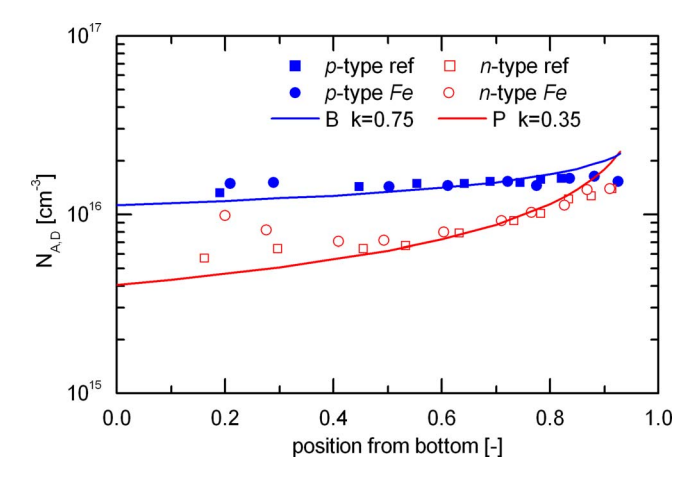


FIG. 2. (Color online) Acceptor and donor concentration for the n-type and p-type ingots vs vertical position in ingot from bottom (bottom: 0 and top: 1). The lines represent the Scheil distribution of B and P where k denotes the distribution coefficient typically found in literature (Refs. 17 and 18).

Fe" and "*n*-type Fe" to refer to the *p*-type and *n*-type multicrystalline silicon ingots intentionally contaminated with Fe.

III. RESULTS

A. Solar cell characterization

The bulk doping level is reported in Fig. 2. The lines represent the Scheil distribution 19 of B and P where the equilibrium distribution coefficient for B [$k_{\rm eq}$ =0.75 (Refs. 17 and 18)] and P [$k_{\rm eq}$ =0.35 (Refs. 17 and 18)] is considered. The bulk resistivity is about 1.0 Ω cm for the p-type ingots and ranging from 0.4 to 0.8 Ω cm for the n-type ingots.

In Fig. 3 the product of the short circuit current (J_{sc}) and the open circuit voltage (V_{oc}) is reported as a function of the vertical position in the ingots. We report the $J_{\rm sc}V_{\rm oc}$ product because this value is more representative of the recombination in the solar cells, excluding the variation present in the fill factor (FF) due to process-induced or material-related series resistance and shunts. Only in the bottom and in the top of p-type Fe ingot and in the top of the n-type reference ingots there is a significant decrease in the FF (shown in Fig. 3). In the p-type ingots, three main regions can be distinguished along the ingot height: (i) the bottom half, (ii) the region around 70% height, and (iii) the top of the ingot. In region (ii) the solar cell performances are comparable for the p-type Fe and p-type reference ingot. In regions (i) and (iii), the bottom half and the top, the cell performances are reduced for the p-type Fe ingot compared to the p-type reference. In the n-type ingots the solar cell performances are reduced in the Fe ingot compared to the reference in regions (i) and (ii). In region (iii), top, the performance of the reference ingot decreases and approaches the Fe ingot.

The IQE (Fig. 4) was derived from spectral response and reflectivity measurements for the p-type and n-type ingots. The IQE curves show that the main differences of the solar cell performance between the reference and Fe doped ingots are in the long wavelength response. The effective average minority carrier diffusion length ($L_{\rm eff}$) was calculated²⁰ from the curve of $1/{\rm IQE}$ versus $1/\alpha(\lambda)$, where $\alpha(\lambda)$ is the absorp-

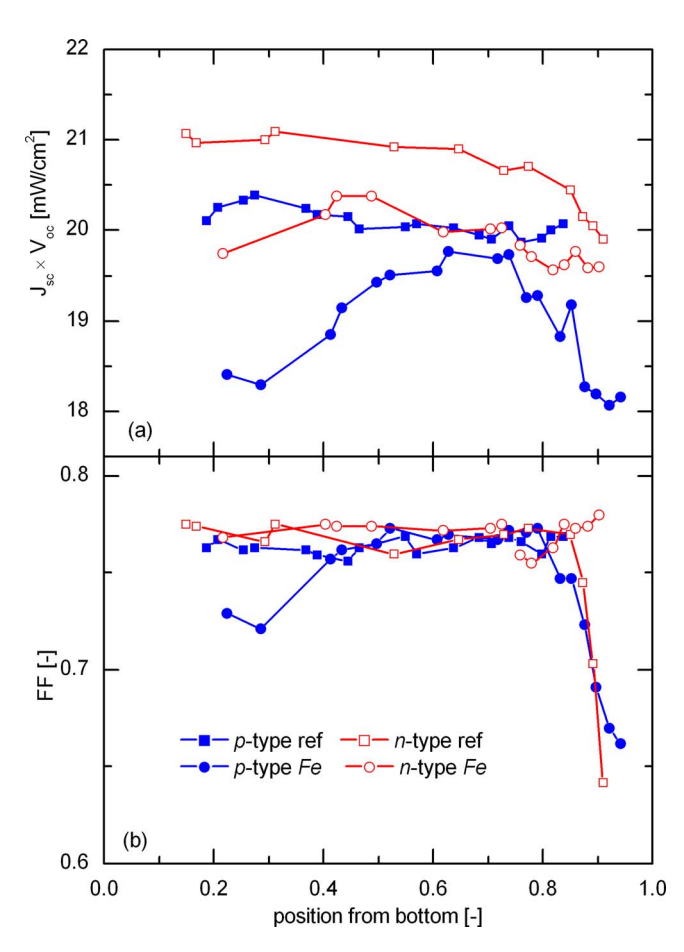


FIG. 3. (Color online) (a) $J_{\rm sc}V_{\rm oc}$ and (b) FF vs vertical position in ingot.

tion length in silicon for wavelength λ . The results are reported in Fig. 5. The diffusion length (L_d) is the limiting factor for the solar cell performance.

The spatial distribution of defects has been investigated by maps of local effective diffusion length obtained combining light beam induced current (LBIC) and reflectance measurements at three different wavelengths over the whole area of the solar cells. These data were converted into maps of internal quantum efficiency and finally to maps of local effective diffusion length, 21 which are shown in Fig. 6. The L_d maps qualitatively represent the grain structure (grains with high defect density give a relatively low LBIC signal and low L_d). Figure 6 shows that there is a difference in the crystal structure development for the Fe ingots compared to the reference ingots. At the bottom and top of the Fe ingots the density of the crystal defects is enhanced, both in comparison to region (ii) in the same ingots and in comparison to the reference ingots. The histograms of L_d (shown in Fig. 7) will be treated in detail in Sec. IV.

B. Minority carrier lifetime changes due to *p*-type and *n*-type solar cell process steps

1. p-type solar cell process

The minority carrier lifetime has been measured by quasi-steady-state photoconductance (QSS-PC) at an injection level of 10¹⁵ cm⁻³ before and after FeB pairs dissociation. ^{23,24} In Fig. 8 the FeB lifetime versus vertical position in the ingot is shown after different *p*-type cell pro-

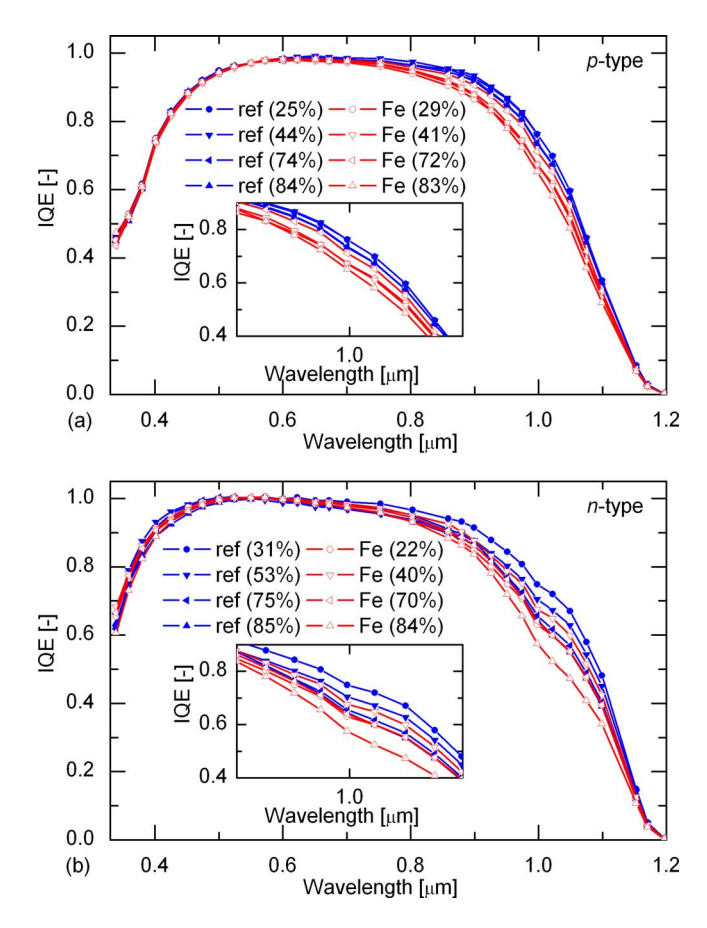


FIG. 4. (Color online) IQE at different heights in the p-type (a) and n-type (b) ingots.

cess steps. The n-type wafers were processed together with the p-type wafers according to Fig. 1. For the p-type reference ingot the as-grown lifetime is good and just a minor improvement is seen after gettering and hydrogenation. In the wafers from this ingot, BO-related light induced degradation affected the minority carrier lifetime already after 60 s illumination (BO degradation is known to occur in mc-Si wafers 25,26). As a result, due to a partial BO-related defect

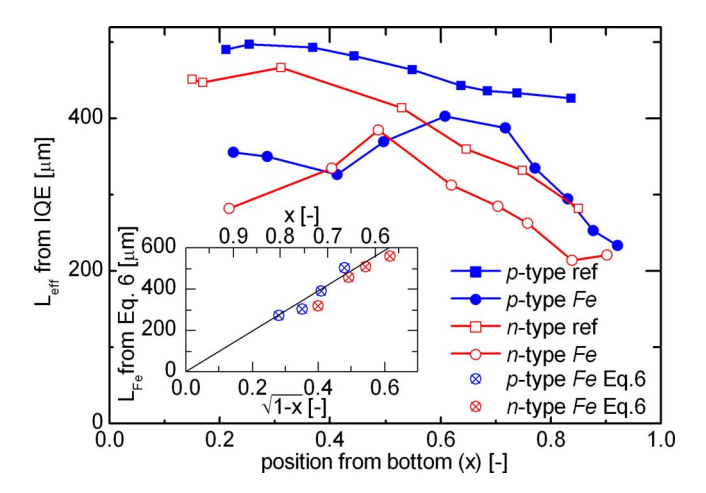


FIG. 5. (Color online) Diffusion lengths in the reference p- and n-type ingots and Fe doped p- and n-type ingots vs vertical position. In the inset, the diffusion length relative to Fe is plotted vs square root of the vertical position from the ingot top.

formation during the QSS-PC measurements, the lifetime for the *p*-type reference wafers reported in Fig. 8 is slightly underestimated.

The as-grown lifetime in p- and n-type Fe doped wafers is about 1–2 and 6–20 μ s, respectively. This difference in lifetime between p and n types can be explained by Shockley–Read–Hall (SRH) model applied to interstitial Fe defects and will be discussed in Sec. IV C. The improvement of lifetime after gettering and hydrogenation of the p-type Fe ingot is up to 50 times and of the n-type Fe ingot five times in the center of the ingot. After gettering and hydrogenation the lifetimes in the n- and p-type Fe doped ingots are approaching each other (lifetime is about two times higher in the n-type than in the p-type ingot). As-grown lifetime values for the n-type reference are similar to the gettered values of the n-type Fe ingot (Fig. 8).

2. n-type solar cell process

In Fig. 8 the lifetime versus vertical position in the ingot is shown after gettering and hydrogenation according to an n-type solar cell process. The p-type wafers were processed together with the n type in the n-type cell process described in Sec. II. The improvements of lifetime after B/P codiffusion and hydrogenation are up to ten times and three to ten times for the p-type Fe and n-type Fe ingots, respectively. The lifetime in the n-type Fe ingot is up to eight times higher than the p-type Fe ingot after gettering and hydrogenation.

3. Interstitial iron concentration

In order to quantify the gettering effectiveness by another parameter than lifetime, the interstitial Fe (Fe_i) concentration was derived from lifetime measurements before and after FeB pair dissociation, ²⁴ only for the *p*-type ingots. In Fig. 9 the interstitial Fe concentration is shown versus vertical position in the *p*-type Fe ingot. The as-grown [Fe_i] is about 10^{13} cm⁻³ in the middle of the ingot and decreases to about 10^{11} cm⁻³ after phosphorous diffusion. After subsequent hydrogenation active [Fe_i] is further reduced by a factor 2. The concentration of Fe_i after B/P codiffusion and hydrogenation is about 10^{12} cm⁻³. The [Fe_i] of as-grown wafers are indicative since the lifetime of these wafers is very low $(1-2 \ \mu s)$, which reduces the measurement accuracy ([Fe_i] is derived from a very small change in lifetime, and dissociation is more difficult to accomplish).

IV. DISCUSSION

In this section the results are discussed separately by topic. In the first paragraph (Sec. IV A) the reduced performance of the solar cells are analyzed discussing the different contributions to the diffusion length reduction. The following paragraph investigates the spatial distribution of crystal defects and shows interaction with the contamination of Fe. At last the minority carrier lifetime and interstitial Fe concentration at different stage of the solar cell process are discussed in Sec. IV C.

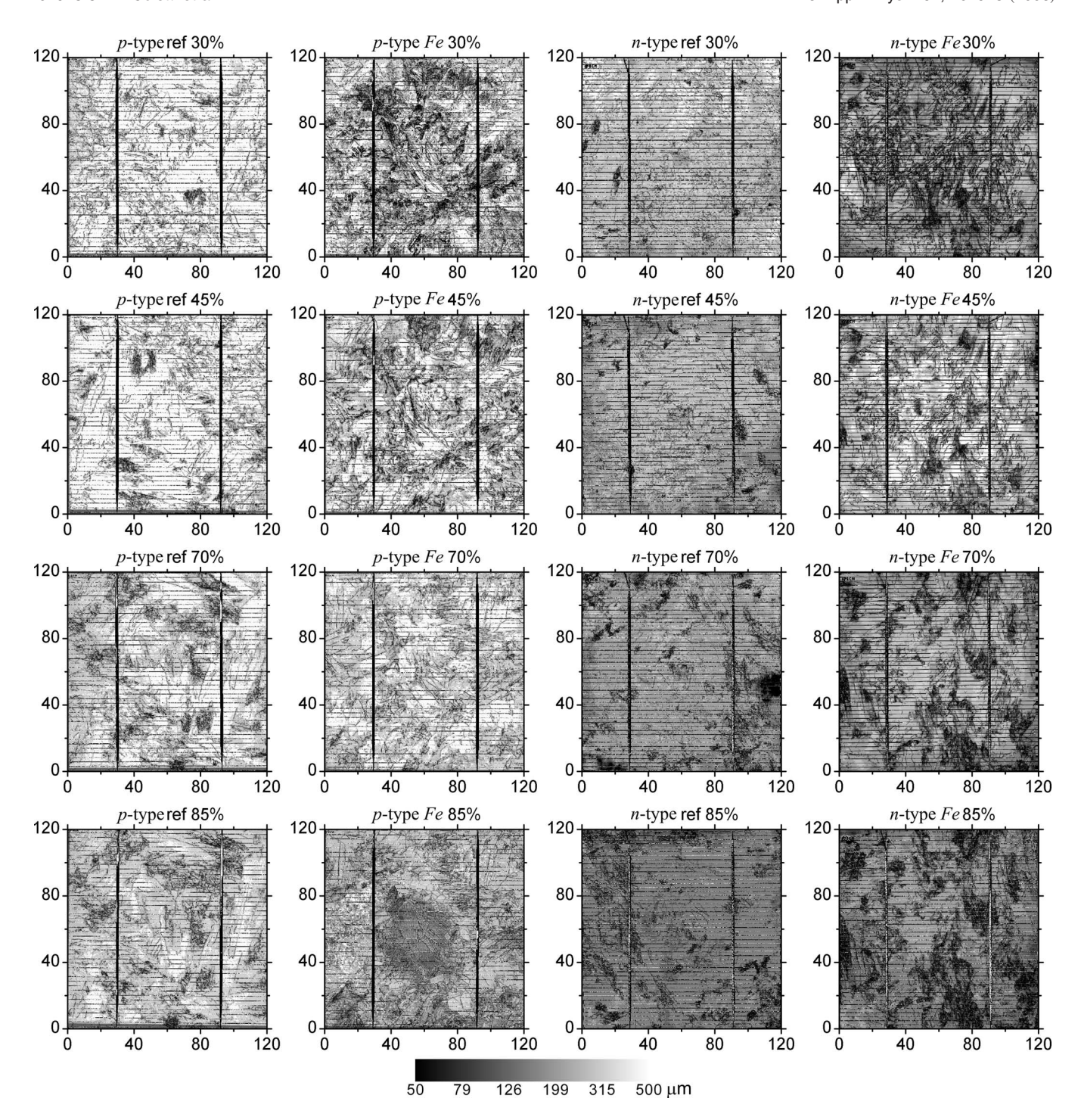


FIG. 6. L_d maps at 30% (upper pictures), 45%, 70%, and 85% (lower pictures) of the ingot height. Most left: p-type reference ingot. Centre left: p-type Fe ingot. Centre right: n-type reference ingot. Most right: n-type Fe ingot. The x-y axis values are given in mm.

A. Solar cells

The addition of 53 ppm by weight Fe to the feedstock causes an overall lowering of solar cell performance compared to the reference. The performance is, however, remarkably close to the reference at positions between about 60% and 70% of the ingot height for the p-type ingots. In the n-type ingot, the addition of Fe reduces the solar cell performance in most of the ingot. The main reason for the degradation is a reduction in the diffusion length (Fig. 5).

In the n-type ingots, the Fe contamination results in a decrease in $V_{\rm oc}$ which could not be fully explained by a

lower diffusion length in the bulk in one-dimensional cell modeling (Ref. 27). $V_{\rm oc}$ decrease may be related either to the contamination of the emitter or to the spatial inhomogeneity in the bulk properties. However, an increase in recombination in the emitter region is not visible in the IQE measurements at short wavelengths (Fig. 4) differently than reported by Macdonald *et al.*²⁸ Further experimental work is needed in order to discriminate between the possible causes.

In the *n*-type reference, the significant decrease in the FF in top can be related to the high substitutional carbon concentration found in the top region (see Sec. II). The impact of

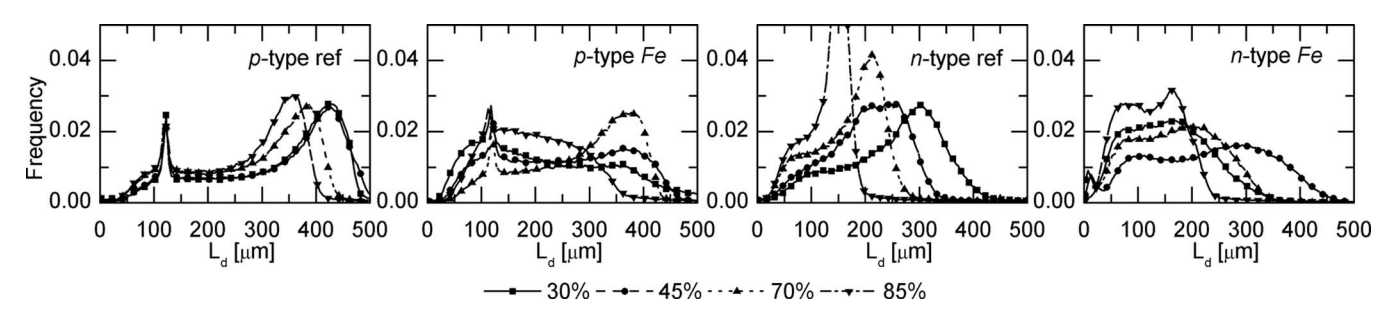


FIG. 7. Histograms of L_d maps shown in Fig. 6.

carbon on the solar cell performance is not completely known;²⁹ however, SiC precipitates are known to cause shunt in the solar cell.^{30–32}

In order to analyze the different contributions to the reduction in the diffusion length, we compare L_d with the expected trend for a metal impurity concentration in the ingot. The equation describing the diffusion length as a function of lifetime (τ) is

$$L_d = \sqrt{D\tau},\tag{1}$$

the lifetime as a function of point defect density (N_t) is

$$\tau \propto \frac{1}{N_t},$$
 (2)

and the Scheil equation describing the segregation of impurities is

$$N_t = \beta C_s = \beta k C_0 (1 - x)^{(k-1)}, \tag{3}$$

where C_s is the total impurity concentration, k is the distribution coefficient, and x is the fractional ingot height from bottom $(0 \le x \le 1)$. β is the percentage of total impurity which is electrically active as point defect. Combining Eqs. (1)–(3) gives the following relation to be expected for diffu-

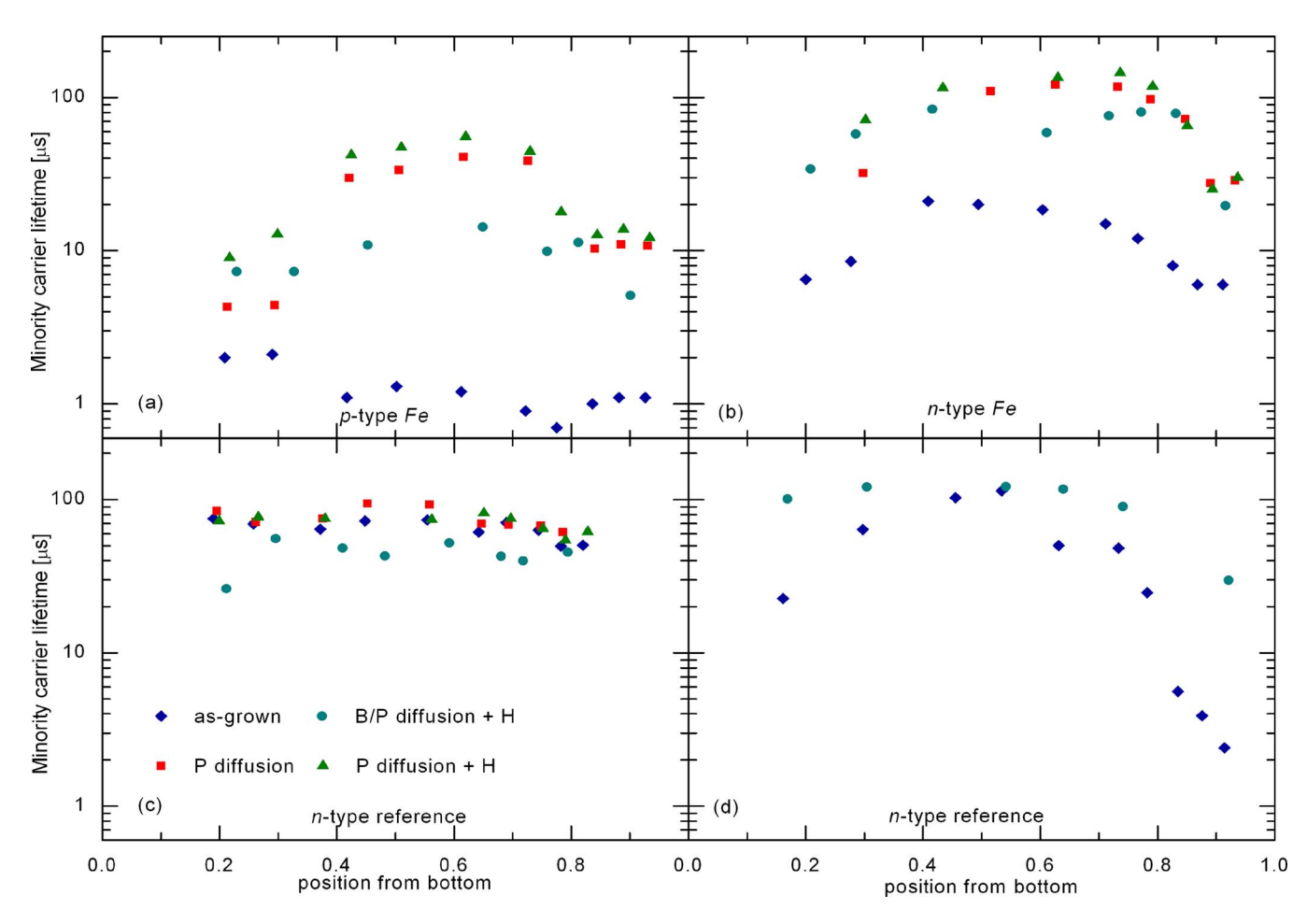


FIG. 8. (Color online) Minority carrier lifetime vs vertical position in the ingots. The data are reported after different solar cell process steps. P diffusion: emitter formation in p-type solar cell process. P diffusion+H: emitter formation, SiN_x :H deposition, and firing as in the p-type solar cell process. B/P codiffusion+H: emitter and BSF formation, SiN_x :H deposition, and firing as in the n-type solar cell process. (a) p-type Fe doped. (b) n-type Fe doped. (c) p-type reference.

FIG. 9. (Color online) Interstitial Fe concentration vs vertical position in p-type Fe doped ingot. The data are reported after different solar cell process steps. $[Fe_i]$ was derived from lifetime measurements before and after FeB dissociation. In the inset $[Fe_i]$ is reported vs vertical position from the top. The lines in the inset are Scheil equation fits [Eq. (3)] to the measured data with k < 0.01 (for all k < 0.01 the slope of the curves does not noticeably depend on k anymore).

sion length as a function of position in ingots dominated by metal point defects,

$$L_d \propto \sqrt{1-x}.\tag{4}$$

The diffusion length in the *p*-type reference is relatively flat (see Fig. 5) where only a slight decrease in diffusion length toward the top of the ingot is observed. This could mean that the transition metals distribution effect [Eq. (3)] is small compared to other causes for reduction in lifetime, such as recombination at crystal defects (e.g., dislocations and grain boundaries).

In order to isolate the impact of Fe, the total recombination in the Fe ingots $(1/\tau_{\rm eff})$ can be approximated as the impact of added Fe $(1/\tau_{\rm Fe})$ plus the impact of crystal defects $(1/\tau_{\rm crystal\ defect})$,

$$\frac{1}{\tau_{\text{eff}}} = \frac{1}{\tau_{\text{Fe}}} + \frac{1}{\tau_{\text{crystal defect}}}.$$
 (5)

We use the reference ingot to estimate $\tau_{\text{crystal defect}}$. Indeed this assumes that the impact of the added Fe does not change the recombination due to the crystal structure. We will see later that this assumption may not be valid in parts of the ingot. Using Eq. (1) gives then

$$\frac{1}{L_{\text{Fe}}^2} = \frac{1}{L_{\text{eff}}^2} - \frac{1}{L_{\text{ref}}^2}.$$
 (6)

The Fe dependent diffusion length $(L_{\rm Fe})$ versus $\sqrt{1-x}$ is included in the inset of Fig. 5. This diffusion length, in both Fe ingots, shows a linear trend with $\sqrt{1-x}$ in the top half of the ingots. This means that L_d is limited by a mechanism which

is governed by the Scheil equation, such as the segregation of Fe in the solid silicon. The interpretation of this result is discussed, together with the distribution of $[Fe_i]$, at the end of Sec. IV C. Clearly, the calculation of L_{Fe} using Eq. (6) becomes inaccurate when L_{eff} and L_{ref} are close.

B. Crystal structure

The L_d maps (see Fig. 6) show grain structures which are significantly different in the Fe ingots compared to the references and with a significant change occurring within the Fe ingots themselves. In order to study this structure we discriminate between low and high recombination areas. High recombination areas correspond qualitatively to grain boundaries (GBs) and dislocations and quantitatively to areas with L_d around 100 μ m in the histograms of Fig. 7. Low recombination areas correspond to the intragrain regions (L_d around 400 μ m in the histograms of Fig. 7).

In the n-type ingots, both the reference and Fe doped ingots, there is a reduction in L_d in the intragrain areas going from the bottom to the top of the ingots. The same behavior is present, but much less evident, in the p-type reference ingot. The most harmful impurities in n-type wafers are mainly substitutional and thus have a low diffusivity. The higher evidence of impurity segregation in n-type cells may be related to less effective gettering due to this low diffusivity of "important" impurities, as well as due to the B/P codiffusion taking place at higher temperature in the cell process.

In the bottom and at the top of both Fe ingots, there are more low L_d areas, which correspond to GBs and dislocations. This is evident from the histograms (see Fig. 7). The area of low L_d decreases from the bottom to the center and then increases again toward the top. Both the reference ingots have lower low- L_d areas and comparable crystal structure from bottom to top. The L_d distribution (Fig. 7) at about 70% height of the p-type Fe ingot is comparable to that of the p-type reference. Note that the solar cell performances are comparable as well at this height.

The addition of Fe in the p- and n-type ingots causes a decrease in the diffusion length in top of the ingots due to segregation and increase in dissolved metal impurities. Our results indicate that this is, however, not the only effect of the high levels of Fe. The increased crystal defect concentration in the top and bottom of the ingots (represented by the low- L_d peaks in the histograms in Fig. 7) contributes considerably to solar cell performance degradation. We believe these are also related to the Fe contamination. The increasing defect concentration in the top of the ingots may be related to the increasing iron concentration in the melt (due to the segregation) that affects the growth process. A known example of the impact of impurity concentration on the crystal growth is the constitutional supercooling, as observed earlier on intentionally contaminated ingots. 34,35 In our case, however, the effect is not as severe as constitutional supercooling. In the bottom of the ingot, the high concentration of Fe in the silicon melt may have initiated or enhanced a disturbance of nucleation and growth during the early solidification phase. Although it is known from practice that the initial phase of

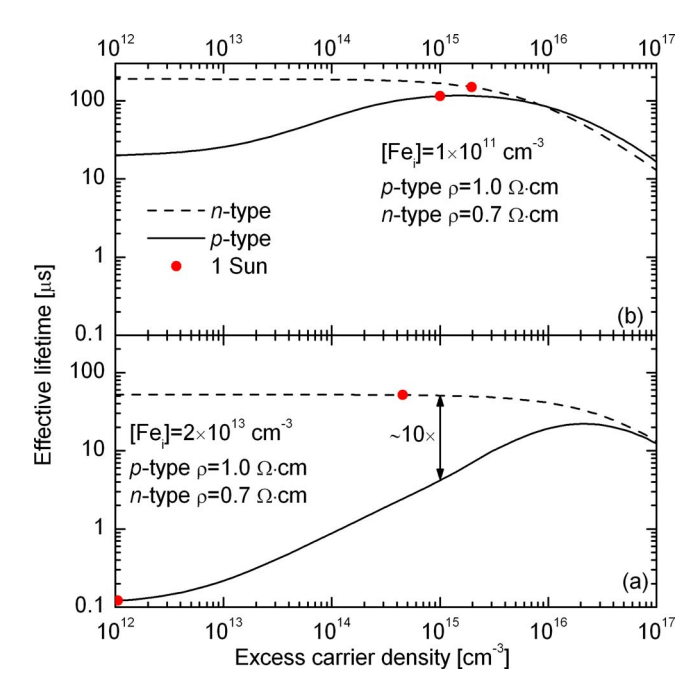


FIG. 10. (Color online) Injection level dependent lifetime in p-type and n-type due to Fe $_i$. (a) [Fe $_i$]=2×10¹³ cm⁻³ as measured in as-grown p-type wafers. (b) [Fe $_i$]=1×10¹¹ cm⁻³ as measured after P diffusion and hydrogenation in p-type wafers. An emitter recombination current (J_{0e}) of 1 ×10⁻¹³ A/cm² has been used. The band to band and Auger recombination were considered (Ref. 37).

ingot growth is susceptible to disturbances, literature on this phenomenon is scarce. Verification of the hypothesis that the increased crystal defect density in the bottom of the Fe doped ingots is related to the high Fe concentration would require additional dedicated experiments and modeling.

C. Minority carrier lifetime

In this paragraph we consider the impact of the Fe introduced in p- and n-type ingots on the lifetime at different stages of the solar cell process. The interstitial iron variations are discussed in the last paragraph. The interstitial Fe capture cross section for electrons is nearly three orders of magnitude higher than for holes.³⁶ However, the as-grown lifetime in n-type Fe ingot is only one order of magnitude higher than

TABLE II. Minority carrier lifetime improvements compared to as-grown after diffusion and hydrogenation in the center of the ingot.

Process	p-type Fe wafers	n-type Fe wafers
P diffusion+hydrogenation	$\sim 50x$	$\sim 5x$
B/P codiffusion+hydrogenation	$\sim 10x$	$\sim 4x$

in the p type (see Fig. 8) at an injection level of 10^{15} cm⁻³. This is much less than the Fe capture cross section ratio for electrons and holes. However, taking in consideration the injection level at which the lifetime has been measured and the Fe concentration, the SRH curves appropriate for the p-type wafers already significantly bend upward (see Fig. 10). At 10^{15} cm⁻³ the lifetime in the p and n types differ by a factor of 10 in agreement with experimental data. The difference between *n*-type and *p*-type lifetimes in the Fe doped ingots can be explained by the physical properties of iron. In order to predict the effect of Fe in p- and n-type cells, it is important to know the injection level at the solar cell working condition. After gettering, the amount of Fe is reduced and so is the overall recombination. Therefore the injection level increases and the gap between n-type and p-type SRH lifetime curves decreases. In particular the emitter recombination current and the Auger recombination³⁷ become dominant and the lifetime is similar as shown in Fig. 11. However, in case other recombination mechanisms are present, the injection level is lower and the gap n or p type increases.

After diffusion and hydrogenation the lifetime of both p-type and n-type Fe doped ingots increases. In Table II the lifetime improvement after diffusion and hydrogenation of p-type and n-type cell processes is summarized. The most harmful impurities in n-type wafers are mainly substitutional. The reduced gettering effectiveness of the p-type cell process (i.e., the phosphorus diffusion) in n-type wafers compared to p-type wafers might be explained by the presence of nongetterable defects, such as substitutional impurities. However the surface passivation might also limit the lifetime in the n-type wafers (see Sec. II).

The lifetime improvement on *p*-type wafers is reduced with the B/P codiffusion compared to the phosphorous diffu-

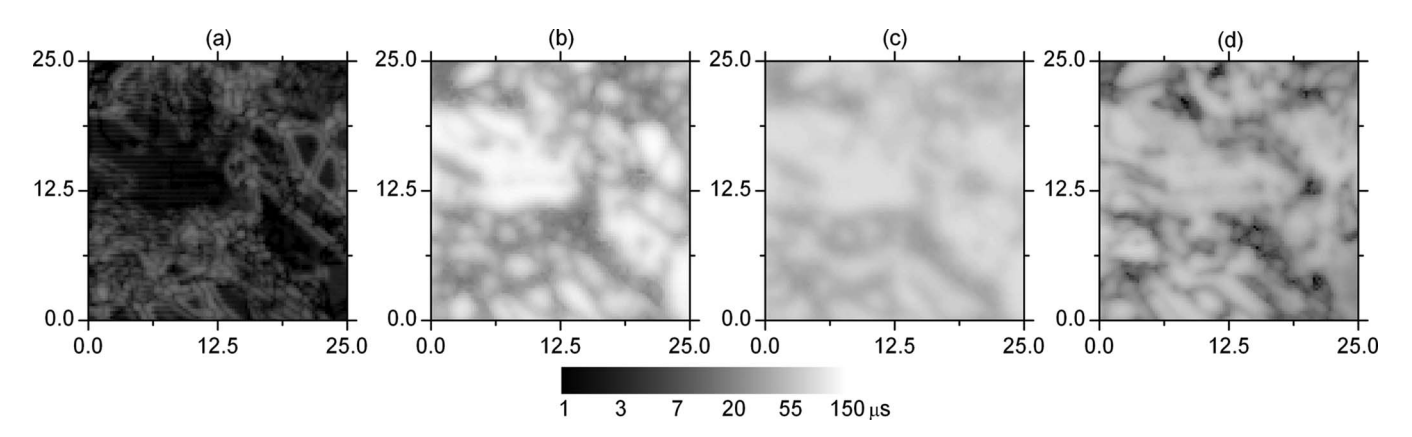


FIG. 11. Lifetime map as measured by modulated free carrier absorption (Ref. 38) on neighboring wafers at \sim 75% height of the *p*-type Fe ingot. The resolution used is 250 μ m. The as-grown sample (a) has been illuminated with a bias light of 25 suns. Most of the traps are filled at this corresponding injection level as determined by QSS-PC measurements. The samples after P diffusion (b), P diffusion+hydrogenation (c), and B/P codiffusion+hydrogenation (d) have been illuminated with a bias light of 2.5 suns.

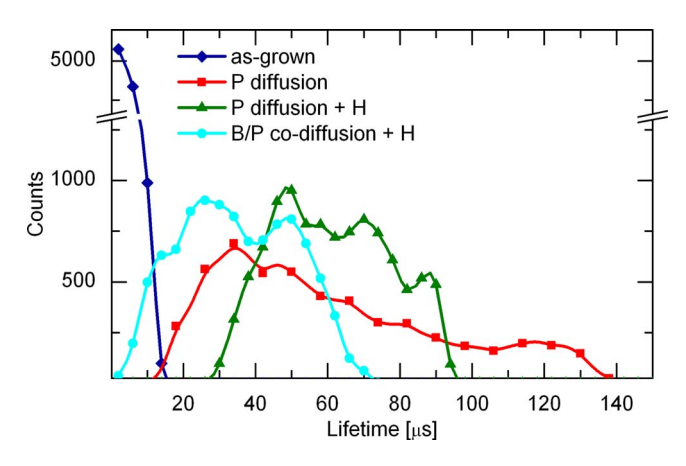


FIG. 12. (Color online) Lifetime distribution after different solar cell process step.

sion. The gettering by boron diffusion is less effective than the phosphorous diffusion.²⁸ In addition B/P codiffusion takes place at a higher temperature which is not the optimal temperature for gettering^{39,40} and a larger amount of impurities can dissolve from precipitates and diffuse.

1. Lifetime in the p-type versus n-type solar cell process

The lifetime maps can give more insight in the local variation of recombination centers in these experiments and particularly for Fe. The lifetime spatial distribution after several solar cell process steps has been investigated by means of modulated free carrier absorption³⁸ technique. In Fig. 11 the lifetime maps of neighboring wafers from the middle of the p-type Fe ingot are shown after each solar cell process step (as grown, after diffusion, and after hydrogenation). The as-grown samples have been measured with a bias light intensity of 25 suns also to avoid minority carrier trapping artifact, and the samples after phosphorous diffusion and hydrogenation have been measured with 2.5 suns. The asgrown lifetime map shows several GBs rimmed, along their length, by higher lifetime boundaries. QSS-PC lifetime measurement shows that most of the traps are filled at 25 suns illumination. The higher lifetime reported is not due to trapping. GBs can act as sink for impurities (also known as internal gettering^{35,41,42}), which cause an impurity depletion region beside the GBs. It should be noted that higher lifetime is visible close to GBs while intragrain areas have the lowest lifetime.

The maps show that the lifetime increases extremely after phosphorous diffusion especially in the intragrain areas. After hydrogenation the darker areas improve, showing the passivation of defect areas (GBs and areas with high dislocation density). On the other hand, in the higher lifetime areas, which correspond to intragrain areas, the lifetimes slightly decrease. The degradation of intragrain areas after hydrogenation is observable also in different material in an earlier work but not discussed. In this areas, the high lifetime (>100 μ s) can also be limited by the surfaces recombination. The overall impact of hydrogenation is visible in the histogram of Fig. 12, where the lifetime distribution is reduced at high lifetime after hydrogenation. On the other

hand, the low lifetime distribution improves. The $1/\tau$ averaged lifetime increases from 47 to 58 μ s after hydrogenation, confirming the beneficial effect of the hydrogenation. As a reference, the as-grown $1/\tau$ averaged lifetime is 2.4 μ s.

The lifetime distribution after B/P codiffusion and hydrogenation has the same shape of the distribution after phosphorous diffusion and hydrogenation but the entire curve is shifted toward low lifetime for the B/P codiffusion. The lifetime map of this sample looks less homogeneous and several crystal defects, hardly visible in the phosphorous diffusion wafer, are still active. The passivation of GBs, and crystal defects in general, depends on the GBs character and impurity level. Since the samples are neighboring, the GBs character and as-grown impurity distribution and precipitates are similar. The activity of the crystal defects is, therefore, due to the higher impurity level after the B/P codiffusion compared to the phosphorous diffusion.

2. Interstitial iron concentration

From Eq. (3) and by knowing the $[Fe_i]$ in the as-grown wafers it is possible to calculate the percentage of total Fe which is electrically active (β) after the ingot crystallization. We fit the experimental data in Fig. 9 considering the initial Fe concentration (C_0) in the silicon melt (the Fe introduced, 53 ppm by weight), the effective distribution coefficient of 2×10^{-5} for Fe in the *p*-type Fe ingot determined by means of NAA and glow-discharge mass spectroscopy analyses in Ref. 9, and β as a fit parameter. As a result β =0.1, i.e., the Fe_i concentration is about 10% of the total concentration of Fe

The active [Fe_i] after hydrogenation is reduced by a factor of two in the p-type Fe ingot, as shown in Fig. 9. An earlier study has shown the passivation of Fe by means of hydrogen. ⁴⁸ The determination of $[Fe_i]$ by means of lifetime measurements is, however, affected by lifetime inhomogeneity. This results in an overestimation of the [Fe_i] depending on the level of inhomogeneity, ²³ as in the sample after gettering [Fig. 11(b)]. An estimation of the magnitude of this effect is not trivial. As an example, a lifetime inhomogeneity of 50% (50% of the total area has good lifetime and 50% bad lifetime) can cause an overestimation in the $[Fe_i]$ by a factor of 2. The concentration of [Fe_i] after hydrogenation is lower by more than one order of magnitude in the phosphorous diffused wafer than in the B/P codiffused wafers (see Fig. 9), confirming the reduced Fe gettering by the B/P codiffusion process.

The inset of Fig. 9 shows the interstitial Fe concentration after different process steps versus position from top for the p-type Fe ingot. The lines in the inset (Fig. 9) are an attempt to fit the Scheil equation (Eq. (3)) to the measured data, using k < 0.01 (for all k < 0.01 the slope of the curves does not noticeably depend on k anymore). The data at the top (>90%) and at the bottom (<20%) are affected by solid-state impurity diffusion during the ingot cooling and by the presence of highly dislocated areas which are known to affect the gettering effectiveness.

The concentration of interstitial Fe after phosphorous diffusion, and after diffusion and hydrogenation, is not con-

stant but shows a trend roughly referable to the Scheil equation. This is an interesting and perhaps somewhat surprising result, which is visible on wafer level (lifetime and [Fe] after diffusion and diffusion+hydrogenation) as well as on solar cell level (diffusion length calculated in Sec. IV A). The cause of this trend is uncertain. Impurity gettering is a complex process governed by impurity diffusion to the gettering layer, dissolution of precipitates, and reprecipitation. If the precipitates are not completely dissolved and the sample is cooled fast enough, the concentration of Fe_i should be equal to the solubility of Fe at the gettering temperature.⁴⁰ In a simple approximation, the [Fe_i] after gettering should thus be independent of the wafer position since the gettering is done under the same conditions (thermal profile) for all the wafers. However during the cool down, Fe; can still diffuse, be gettered, or reprecipitate. Indeed the observed [Fe_i] $\sim 10^{11}$ cm⁻³ is lower than the solubility of Fe at the gettering temperature. A more correct description should include the impact of the crystal structure. Toward the top of the ingot the crystal structure gets worse (see Fig. 6). Since the gettering effectiveness is known to depend on the crystal structure, this might explain the observed trend for [Fe_i]. A detailed interpretation of these results is outside the purpose of this paper and requires modeling of precipitate dissolution involving their size and density. To our knowledge a comparison of impurity concentrations with segregation curves after gettering has not been reported before.

V. CONCLUSIONS

53 ppm by weight of Fe has been introduced in the silicon feedstock before the melting and the subsequent solidification of a p-type and an n-type doped ingot. The differences in the as-grown lifetime between p- $(1-2 \mu s)$ and n-type $(6-20 \mu s)$ Fe doped Si ingots are explained with SRH theory for interstitial Fe defects. We observe that some GBs act as sink for impurities, causing a cleaner, higher lifetime region beside these GBs. The as-grown $[Fe_i]$ in the p-type Fe doped ingot is in the order of 10^{13} cm⁻³, which represent about 10% of the total iron concentration.

p-type and n-type solar cell processes were applied both to wafers sliced from the Fe doped ingots and reference ingots produced from non-Fe doped silicon feedstock. After phosphorous diffusion and hydrogenation, the improvement of lifetime is up to 50 times for the p-type Fe doped ingot and 5 times for the n-type Fe doped ingot. After boron/phosphorus codiffusion and hydrogenation the improvement is about 10 times for the p-type ingot and about 4 times for the n-type ingot. The [Fe $_i$] drops from about 10^{13} cm⁻³ to about 10^{11} cm⁻³ in the p-type Fe ingot after phosphorous diffusion. The concentration of Fe $_i$ after B/P codiffusion and hydrogenation is about 10^{12} cm⁻³, which confirms the reduced Fe gettering of the B/P codiffusion process.

The concentration of interstitial Fe after the solar cell processing (P diffusion and hydrogenation) shows a trend along the ingot which roughly follows the Scheil equation. A decrease of the solar cell diffusion length, which can be ascribed to a Scheil-like distribution of active Fe is observed as

well. Passivation of GBs and areas with high dislocation density by means of hydrogenation is observed.

There is a difference in the crystal structure development for both the Fe doped ingots compared to the reference ingots. At the bottom and at the top of the Fe doped ingots the density of the crystal defects is enhanced, both in comparison to about 70% height within the same ingots and in comparison to the reference ingots. This is reflected in the solar cell efficiencies, which are reduced in the bottom and top, but are comparable to the reference at around 70% height.

The increasing defect concentration in the top of the Fe doped ingots may be related to the increasing iron concentration in the melt. In the bottom, the initial high concentration of Fe in the silicon melt may have originated a transient nucleation and growth disturbance during the early solidification phase.

ACKNOWLEDGMENTS

The authors would like to thank the European Projects "Foxy-Development of Solar-Grade Silicon Feedstock for Crystalline Wafers and Cells by Purification and Crystallisation" (Grant No. SES6-019811) and "CrystalClear Integrated Project" (Grant No. SES6-CT_2003-502583) for financial support. Parts of the work have been supported by the project "Crystalline silicon solar cells—Cost reduction" and funding from the industrial partners and the Norwegian Research Council (Contract. No. 153207/210) is greatly acknowledged. The authors would like to thank the staff at ECN for technical assistance in the experiments. The content is the responsibility of the authors.

¹J. R. Davis, A. Rohatgi, R. H. Hopkins, P. D. Blais, P. Rai-Choudhury, J. R. McCormick, and H. C. Mollenkopf, IEEE Trans. Electron Devices **27**, 677 (1980).

A. A. Istratov, T. Buonassisi, R. J. McDonald, A. R. Smith, R. Schindler, J. A. Rand, J. P. Kalejs, and E. R. Weber, J. Appl. Phys. 94, 6552 (2003).
D. Macdonald, A. Cuevas, A. Kinomura, Y. Nakano, and L. J. Geerligs, J. Appl. Phys. 97, 033523 (2005).

⁴A. A. Istratov, H. Hieslmair, and E. R. Weber, Appl. Phys. A: Mater. Sci. Process. A70, 489 (2000).

⁵C. C. Swanson, A. J. Filo, and J. P. Lavine, J. Radioanal. Nucl. Chem. **248**, 69 (2001)

⁶E. R. Weber, Appl. Phys. A **A30**, 1 (1983).

S. Dubois, O. Palais, P. J. Ribeyron, N. Enjalbert, M. Pasquinelli, and S. Martinuzzi, J. Appl. Phys. **102**, 083525 (2007).

⁸D. Macdonald, H. Mäckel, and A. Cuevas, Appl. Phys. Lett. 88, 092105 (2006).

⁹R. Kvande, L. J. Geerligs, G. Coletti, M. Di Sabatino, E. J. Øvrelid, C. C. Swanson, J. Appl. Phys. **104**, 064805 (2008).

¹⁰Data Sheet, Saint-Gobain Quartz, C10.

¹¹E. Olsen, E. J. Øvrelid, Prog. Photovoltaics 16, 93 (2008).

¹²C. J. J. Tool, M. Koppes, M. Fleuster, B. H. M. van Straaten, and A. W. Weeber, Proceedings of the 21th EUPVSEC, Dresden, Germany, 2006 (unpublished), p. 1272; A. W. Weeber, R. Kinderman, P. C. de Jong, and C. J. J. Tool, Proceedings of the 21th EUPVSEC, Dresden, Germany, 2006 (unpublished), p. 605.

¹³V. D. Mihailetchi, L. J. Geerligs, Y. Komatsu, T. Buck, I. Rover, K. Wambach, C. Knopf, and R. Kopecek, Proceedings of the 22nd European Photovoltaic and Solar Energy Conference, Milan, Italy, 2007 (unpublished).

¹⁴L. J. Geerligs, Y. Komatsu, I. Rover, K. Wambach, I. Yamaga, and T. Saitoh, J. Appl. Phys. **102**, 093702 (2007).

¹⁵I. Romijn, I. Cesar, M. Koppes, E. Kossen, and A. Weeber, Conference Record of the 33rd IEEE Photovoltaic Specialist Conference, San Diego, CA, USA, 2008 (unpublished).

¹⁶J. Libal, Ph.D. thesis, University of Konstanz, p.25.

- ¹⁷H. Dalaker and M. Tangstad, Proceedings of the 22nd European Photovoltaic and Solar Energy Conference, Milan, Italy, 2007 (unpublished), p. 1112 and references therein.
- ¹⁸W. C. O'Mara et al., Handbook of Semiconductor Silicon Technology (Noyes Publications, 1990).
- ¹⁹E. Scheil, Z. Metallk. **34**, 70 (1942).
- ²⁰P. A. Basore, IEEE Trans. Electron Devices **37**, 337 (1990).
- ²¹Semilab Technical Note No. WT-2000.
- ²²B. Sopori, C. Wei, Z. Yi, and J. Madjdpour, J. Cryst. Growth 210, 346 (2000).
- ²³L. J. Geerligs, G. Coletti, and D. Macdonald, Proceedings of the 21st European Photovoltaic Solar Energy Conference, Dresden, Germany, 2006 (unpublished), p. 692.
- ²⁴D. Macdonald, L. J. Geerligs, and A. Azzizi, J. Appl. Phys. **95**, 1021 (2004)
- ²⁵D. Macdonald, L. J. Geerligs, and S. Riepe, Proceedings of the 13th Workshop on Crystalline Silicon Solar Cell Materials and Processing, Colorado, 2003 (unpublished), p. 182.
- ²⁶G. Coletti, C. L. Mulder, G. Galbiati, and L. J. Geerligs, Proceedings of the 21st European Photovoltaic Solar Energy Conference, Dresden, Germany, 2006 (unpublished), p. 1515.
- ²⁷D. A. Clugston and P. A. Basore, Conference Record of the 26th IEEE Photovoltaic Specialist Conference, Anaheim, CA, USA, 1997 (unpublished), p. 207.
- ²⁸D. Macdonald, H. Mäckel, and A. Cuevas, Proceedings of the Fourth World Conference on Photovoltaic Energy Conversion, Hawaii, USA, 2006 (unpublished), p. 952.
- ²⁹L. J. Geerligs, P. Manshanden, G. P. Wyers, E. J. Øvrelid, O. S. Raaness, A. N. Waernes, and B. Wiersma, Proceedings of the 20th EUPVSEC, Barcelona, Spain, 2005 (unpublished), p. 619.
- ³⁰J. Bauer, O. Breitenstein, M. Becker, and J. Lenzner, Proceedings of the 17th Workshop on Crystalline Silicon Solar Cell Materials and Processes, Vail, Colorado, 2007 (unpublished).
- ³¹M. H. Al Rifai, O. Breitenstein, J. P. Rakotoniaina, M. Werner, A. Kaminski, and M. Le Quang, Proceedings of the 19th EUPVSEC, Paris, France, 2004 (unpublished), p. 632.
- ³²A.-K. Søiland, E. J. Øvrelid, O. Lohne, J. K. Tuset, T. A. Engh, and Ø. Gjerstad, Proceedings of the 19th EUPVSEC, Paris, France, 2004 (unpub-

- lished), p. 911.
- ³³D. Macdonald and L. J. Geerligs, Appl. Phys. Lett. **85**, 4061 (2004).
- ³⁴T. F. Ciszek, T. H. Wang, R. K. Ahrenkiel, and R. Matson, Conference Record of the 25th IEEE Photovoltaic Specialist Conference, Washington, DC, 1996 (unpublished), p. 737.
- ³⁵R.H. Hopkins, J.R. Davis, A. Rohatgi, M.H. Hanes, and P. Rai-Choudhury, DOE/JPL Report No. 954331-82/13, 1982.
- ³⁶D. Macdonald, T. Roth, P. N. K. Deenapanray, T. Trupke, and R. A. Bardos, Appl. Phys. Lett. 89, 142107 (2006).
- ³⁷M. J. Kerr and A. Cuevas, J. Appl. Phys. **91**, 2473 (2002).
- ³⁸ A. Schönecker, J. A. Eikelboom, A. R. Burgers, P. Lölgen, C. Leguijt, and W. C. Sinke, J. Appl. Phys. **79**, 1497 (1996).
- ³⁹P. Manshanden, L.J. Geerligs, Sol. Energy Mater. Sol. Cells 90, 998 (2006) and references therein.
- ⁴⁰P. S. Plekhanov, R. Gafiteanu, U. M. Gösele, and T. Y. Tan, J. Appl. Phys. 86, 2453 (1999).
- ⁴¹T. Buonassisi, A. A. Istratov, M. D. Pickett, and M. A. Marcus, Appl. Phys. Lett. **89**, 042102 (2006).
- ⁴²J. Lu, M. Wagener, G. Rozgonyi, J. Rand, and R. Jonczyk, J. Appl. Phys. 94, 140 (2003).
- ⁴³M. Rinio, M. Kaes, G. Hahn, and D. Borchert, Proceedings of the 21st European Photovoltaic and Solar Energy Conference, Dresden, Germany, 2006 (unpublished), p. 684.
- ⁴⁴J. Tan, A. Cuevas, D. Macdonald, T. Trupke, R. Bardos, K. Roth, Prog. Photovoltaics 16, 129 (2008).
- ⁴⁵B. Sopori, Y. Zhang, and N. M. Ravindra, J. Electron. Mater. 30, 1616 (2001).
- ⁴⁶R. A. Sinton, Proceedings of the Third World Conference on Photovoltaic Energy Conversion, Osaka, Japan, 2003 (unpublished).
- ⁴⁷J. Chen, D. R. Yang, Z. O. Xi, and T. Sekiguchi, Physica B **364**, 162 (2005)
- ⁴⁸K. McLean, C. Morrow, and D. Macdonald, Proceedings of the Fourth World Conference on Photovoltaic Energy Conversion, Hawaii, USA, 2006 (unpublished), p. 1122.
- ⁴⁹B. Sopori, J. Electron. Mater. **31**, 972 (2002).
- ⁵⁰O. Schultz, S. W. Glunz, S. Riepe, and G. P. Willeke, Prog. Photovoltaics 14, 711 (2006).